

Measurements and modeling of ion energy distributions in high-density, radio-frequency biased CF_4 discharges

Mark A. Sobolewski,^{a)} Yicheng Wang, and Amanda Goyette
National Institute of Standards and Technology, Gaithersburg, Maryland 20899-8362

(Received 11 January 2002; accepted for publication 12 February 2002)

Models of ion dynamics in radio-frequency (rf) biased, high-density plasma sheaths are needed to predict ion bombardment energies in plasma simulations. To test these models, we have measured ion energy distributions (IEDs) in pure CF_4 discharges at 1.33 Pa (10 mTorr) in a high-density, inductively coupled plasma reactor, using a mass spectrometer equipped with an ion energy analyzer. IEDs of CF_3^+ , CF_2^+ , CF^+ , and F^+ ions were measured as a function of bias frequency, bias amplitude, and inductive source power. Simultaneous measurements by a capacitive probe and a Faraday cup provide enough information to determine the input parameters of sheath models and allow direct comparison of calculated and measured IEDs. A rigorous and comprehensive test of one numerical sheath model was performed. The model, which includes a complete treatment of time-dependent ion dynamics in the sheath, was found to predict the behavior of measured IEDs to good accuracy over the entire range of bias frequency, including complicated effects that are observed when the ion transit time is comparable to the rf bias period. [DOI: 10.1063/1.1467403]

I. INTRODUCTION

Plasma processes are widely used by industry to deposit and etch films. During plasma processing, substrate wafers exposed to plasmas are bombarded by reactive chemical species and energetic ions, resulting in deposition or etching. The energetic ions often play an important role in deposition processes and they are essential for plasma etching. To obtain optimal results, ion kinetic energies must be carefully controlled. In nearly all modern plasma reactors, this is accomplished by applying radio-frequency (rf) power to the substrate electrode. This rf substrate bias is designed solely to control the ion bombardment energies, independent of the rf or microwave source that generates and sustains the plasma. Nevertheless, despite the widespread use of rf bias and much study, the effects of rf bias on ion energies are still not completely understood. Rigorously validated models that would yield accurate quantitative predictions for ion energy distributions (IEDs) are not available.

rf biasing produces a radio-frequency voltage drop, which usually occurs almost entirely across the plasma sheaths, thin regions at the boundary of the plasma, not across the plasma itself. It is also in the sheaths that ions gain most of their energy. Thus to predict ion energies requires a model for the complicated dynamics of plasma sheaths. At low pressures typical of etching plasmas, ion mean free paths are usually larger than the sheath width, so ion collisions in the sheath can often be neglected. Nevertheless, ion dynamics in collisionless sheaths have complicated time-dependent and frequency-dependent effects that are not fully understood.

Many models of collisionless sheaths¹⁻¹⁵ have been derived, but ion energy distributions predicted by the models often disagree. Furthermore, they have not been sufficiently

tested by experiment. Although the effects of rf bias on ion energies have been measured in many studies,^{4,12,14,16-23} these studies typically do not measure all the input parameters needed by the models, so rigorous comparisons of measurements to model predictions are usually not possible. For example, ion energies depend strongly on sheath voltages, but these are rarely measured. To calculate the sheath width and sheath electric fields, models also require a value for the electron density or the total ion current density, but these parameters are also usually left unmeasured.

In contrast, in this study, we performed a rigorous and comprehensive test of ion energy distributions predicted by one sheath model.¹ By combining ion energy measurements with capacitive probe measurements of sheath voltages and Faraday cup measurements of ion current density, we completely determined all the input parameters of the model, allowing us to directly compare model results and measurements. The tests were performed in a high-density, inductively coupled plasma reactor at a pressure of 1.33 Pa (10 mTorr), low enough that ion collisions in the sheath can be neglected. Unlike previous studies performed in rare gases, which typically contain a single dominant ion, we choose CF_4 , which provides a variety of ionic species of different masses. By varying the rf bias amplitude and frequency as well as the inductive source power, we performed a comprehensive test of model predictions for ion energies, including their dependence on sheath voltage, rf bias frequency, ion current density, and ion mass.

We describe the experiment in Sec. II and the model in Sec. III. Model IEDs and measured IEDs are compared in Sec. IV. Peak energies and average energies are also compared there. In Sec. V the width of model IEDs and measured IEDs are compared with each other and with previous work. Section VI summarizes our conclusions.

^{a)}Electronic mail: sobo@email.nist.gov

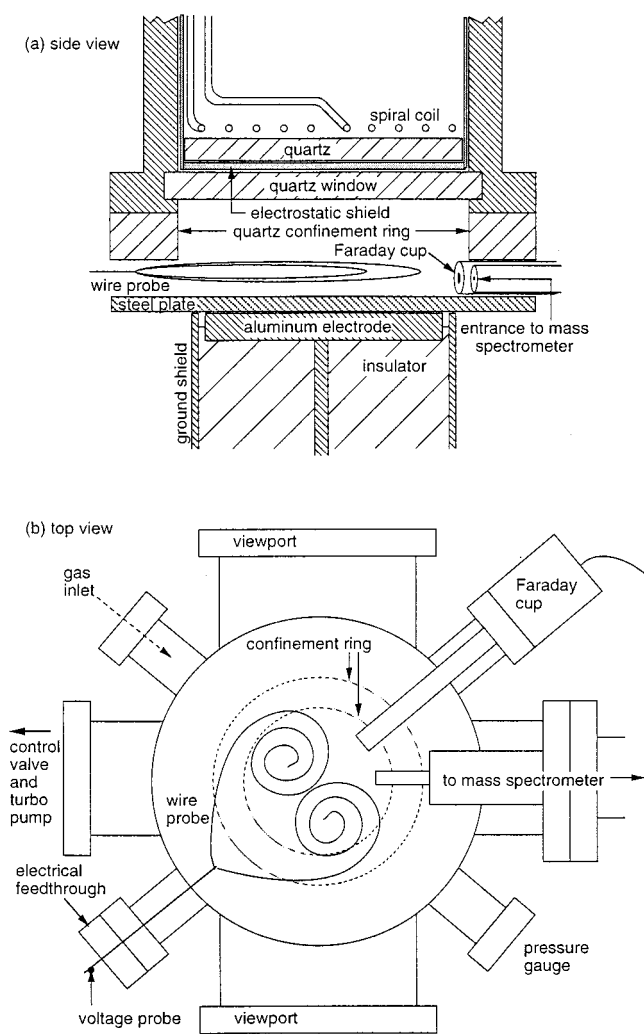


FIG. 1. Diagram of the plasma reactor, including (a) a side view of the electrodes and (b) a top view of the entire chamber. (a) and (b) show two different designs for the wire probe.

II. EXPERIMENT

A. Plasma reactor

Experiments were performed in a Gaseous Electronics Conference (GEC) Reference Cell²⁴ (Fig. 1), in which the standard upper electrode was replaced by an inductive, high-density plasma source. The source²⁵ consists of a five-turn, planar coil with one end grounded and the other end driven by a 13.56 MHz generator and a matching network. The power supplied to the coil was measured at the generator. Therefore reported power values include resistive losses in the matching network and the inductive source. An electrostatic shield²⁶ was placed below the source, insulated from it by a quartz disk. As in Ref. 27, a quartz ring was suspended from the inductive source assembly to help confine the high-density discharge and allow operation in electronegative gases over a broader range of pressure and power.

The lower electrode assembly consists of an aluminum electrode and a steel ground shield, separated by an alumina insulator. As in Ref. 25, a steel plate of diameter 16.5 cm was placed on the lower electrode to increase its effective area and to prevent sputtering of aluminum from the lower elec-

trode onto other cell surfaces. Variable-frequency rf bias was applied to the lower electrode using a signal generator and a power amplifier.

Gas flowed into the cell through a side port of the reactor, shown in Fig. 1(b), at a flow rate of 14.9 $\mu\text{mol/s}$ (20 sccm). The gas outlet was another side port on which a pressure control valve and turbopump were mounted.

B. Mass spectrometer and Faraday cup

Incorporating an ion energy analyzer and mass spectrometer into an rf biased electrode is difficult. The entire instrument must be rf biased, or errors will be introduced.^{10,20} To avoid these difficulties, we instead mounted the energy analyzer/mass spectrometer on a side port, as shown in Fig. 1(b), and grounded its inlet orifice, instead of biasing it. When rf bias is applied to the lower electrode, some rf voltage is developed across the sheath adjacent to the lower electrode, but an additional rf voltage is developed across the ground sheath, i.e., the sheath adjacent to the grounded mass spectrometer inlet and other grounded surfaces. Thus we are still able to study rf bias effects, even though the spectrometer itself is not rf biased.

To sample ions close to the center of the discharge, an extension was attached to the end of the mass spectrometer. It protrudes into the gap between the steel plate and the quartz confinement ring to a distance of 46 mm from the radial center of the reactor, 11 mm inside the inner diameter of the quartz confinement ring. Spot-welded to the end of the extension is a 3.5 μm thick nickel foil, with a 10 μm diameter hole in it, located 9.5 mm above the steel plate. Ions pass through the hole into a cylindrical, field-free region 10 mm in diameter and 42 mm long, and eventually enter the ion energy analyzer and mass spectrometer, which have been described previously.²⁸ The resolution of the energy analyzer [full width at half maximum (FWHM)] was 1 eV, and the uncertainty in its energy scale is estimated to be ± 1 eV. Ion intensities were adjusted to account for previously measured variations in ion transmission as a function of ion mass.²⁸ After such adjustments, the ion transmission is estimated to be uniform to 20% over the range of ion masses and ion energies studied here.

To calibrate the ion fluxes measured by the mass spectrometer, we used a Faraday cup mounted on another side port, next to the mass spectrometer. The 1.59 mm diameter aperture at the inlet of the Faraday cup was positioned at the same radius and height as the mass spectrometer orifice. The dc current measured when the cup was dc biased at -20 V was divided by the area of the aperture to obtain the total ion current density. This value was then used to normalize the relative ion fluxes measured by the mass spectrometer.

C. Capacitive probe

The time-dependent potential in the plasma was measured with a wire probe. We tried two different designs: one consisted of platinum wire coiled into two loops, as shown in Fig. 1(a), the other consisted of steel wire coiled into two spirals, as shown in Fig. 1(b). Both were designed to provide a large area of contact with the intense plasma that fills the region inside the quartz confinement ring. Both were sup-

ported by an electrical feedthrough, a support wire, and connectors described previously.²⁹ The platinum wire was less able to withstand plasma exposure; it gradually grew thinner, presumably by sublimation. The looping of the platinum wire made this problem worse, since the loops allow currents induced by the plasma source to circulate, causing additional heating of the wire. The spiral design is preferred, since it contains no closed loops.

An oscilloscope voltage probe was mounted on the wire probe's electrical feedthrough, outside the vacuum chamber. The oscilloscope digitized the probe signal and transferred the data to a computer, which digitally filtered the signals and extracted the magnitudes and phases of significant Fourier components. In low-density discharges, further analysis is required to account for the rf voltage drop across the sheath that surrounds the wire probe.^{29,30} Here, however, as in previous studies of high-density discharges,^{16,31} the rf voltage across the wire sheath was shown to be negligible. On the other hand, the dc voltage across the wire sheath, V_{bxf} , is not negligible, and must be accounted for. As in Ref. 16, we determined V_{bxf} from ion energy and wire probe measurements made with no rf bias applied. Adding V_{bxf} to the filtered voltage signal, we obtain the complete time-dependent plasma potential, $V_b(t)$, which can also be considered the voltage drop across the sheath in front of the grounded mass spectrometer inlet orifice. Changes in V_{bxf} during the experiments, due to changes in surface conditions or electron temperature, contribute a dc uncertainty in $V_b(t)$, which, for the results presented here, is estimated to be ± 1 V.

III. SHEATH MODEL

A. Model equations

To calculate ion energy distributions we use the same sheath model described in Ref. 1, except for two changes. First, we are now simulating the sheath in front of the grounded mass spectrometer inlet, not the sheath at the rf biased electrode. The coordinate x now indicates the position along the axis perpendicular to the grounded surface. The axis extends from x_0 to x_{ge} , where x_{ge} is the position of the grounded surface and x_0 is an arbitrary position on the plasma side of the sheath. For simplicity, we assume that the inlet orifice is small enough that it does not significantly perturb the sheath electric field or the ion trajectories. Given this assumption, a one-dimensional model is sufficient, and no other position coordinates are needed.

Second, we now allow more than one species of ion in the sheath. The total number of ionic species is N , and the mass of the i th species is denoted m_i . Each species has a single, positive ionic charge, e . Negative ions need not be considered, since they are repelled by the sheath electric field. They remain in the plasma and do not enter the sheath.

The density and mean velocity of the i th ionic species, $n_i(x, t)$ and $u_i(x, t)$, vary with position x and time t according to the fluid equations. At sufficiently low pressures we may ignore ion collisions and ionization within the sheath and write the fluid equations as

$$\partial u_i / \partial t + u_i \partial u_i / \partial x = eE / m_i, \quad (1)$$

and

$$\partial(n_i u_i) / \partial x = -\partial n_i / \partial t, \quad (2)$$

where $E(x, t)$ is the electric field. The field, and the electrostatic potential $V(x, t)$, are related to the total charge density by Gauss's law and Poisson's equation:

$$-\partial V^2 / \partial x^2 = \partial E / \partial x = e(n_+ - n_e) / \epsilon_0, \quad (3)$$

where $n_+(x, t)$ is the total density of all N ionic species, $n_e(x, t)$ is the electron density, and ϵ_0 is the permittivity of vacuum. Voltages are referenced to the grounded surface, i.e., $V(x_{\text{ge}}) \equiv 0$.

We simplify Eq. (3) using the oscillating step approximation,^{32,33} which assumes that the electron density profile has a step-like drop at a time-varying position $W(t)$. On the plasma side of the step $n_e \approx n_+$; on the sheath side, $n_e \ll n_+$. Therefore Eq. (3) becomes

$$-\frac{\partial^2 V}{\partial x^2} = \frac{\partial E}{\partial x} = \begin{cases} 0, & x < W(t) \\ en_+ / \epsilon_0, & x \geq W(t). \end{cases} \quad (4)$$

Using this approach, one avoids having to perform an inefficient, iterative solution for the electron density.

For boundary conditions at $x = x_0$, i.e., at the interface between the plasma and the sheath, we use the following:

$$E(x_0) = 0, \quad (5)$$

$$V(x_0, t) = V_b(t) - 2kT_e / e, \quad (6)$$

$$(1/2)m_i u_i^2(x_0) = 2kT_e, \quad (7)$$

and

$$n_i(x_0) = J_i / [e u_i(x_0)], \quad (8)$$

where $V_b(t)$ is the voltage in the center of the plasma, k is Boltzmann's constant, T_e is the electron temperature, and J_i is the current density of the i th ionic species, time-averaged over one rf cycle. These boundary conditions are chosen so that, for a dc sheath, the step model gives values of E , V , u_i , and n_i at the grounded electrode that agree with Bohm's theory,³⁴ after adapting it to account for multiple ionic species.³⁵ The unexpected factors of 2 in the right-hand side of Eqs. (6) and (7) arise because we match the Bohm theory at the electrode, not at the plasma/sheath boundary. For more discussion, see Refs. 1 and 36.

B. Model input parameters

The sheath model requires a value for the mass m_i and the time-averaged current density J_i of each ionic species. Only the four or five most prevalent ions identified in ion mass scans (Fig. 2) were included. Additional ions, which contributed a few percent or less of the total ion flux, were neglected. To obtain values for J_i , we first determined relative current densities by integrating ion energy distributions measured with no rf bias. Then these relative densities were

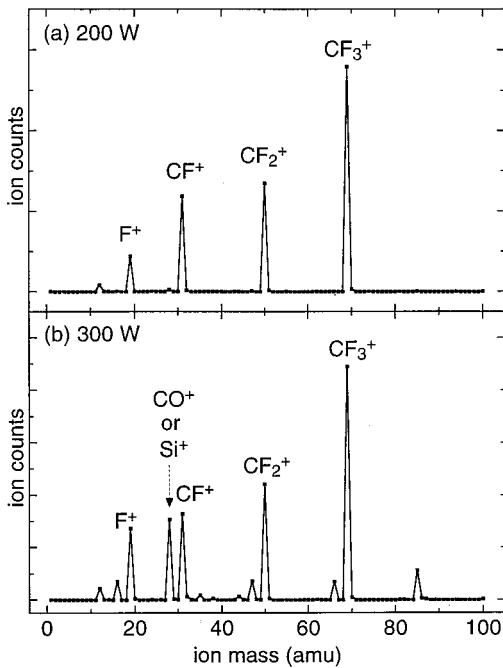


FIG. 2. Ion mass scans for discharges in CF_4 at 1.33 Pa (10 mTorr), no rf bias, and inductive source powers of (a) 200 W and (b) 300 W. The identify of the four or five most prevalent species are indicated. The mass 28 peak in (b), either Si^+ or CO^+ , presumably results from etching of the quartz window under the inductive plasma source. The window was exposed in (b), but in (a) was covered by a layer of material that had been sputtered off of other surfaces.

scaled so that their sum was equal to the total ion current density measured by the Faraday cup. At 200 W inductive source power, the resulting values for J_i were 0.50, 0.34, 0.30, and 0.14 mA/cm^2 for ion masses of 69, 50, 31, and 19 amu, respectively. At 300 W, J_i was 0.92, 0.46, 0.35, 0.30, and 0.28 mA/cm^2 for $m_i=69, 50, 31, 28,$ and 19 amu, respectively.

The model also requires the plasma potential $V_b(t)$, which was determined by the capacitive probe measurements described in Sec. II C, and the electron temperature T_e . For T_e , we used a value of 4.58 eV measured by Singh and Graves³⁷ in a high-density, inductively coupled discharge in pure CF_4 at 1.33 Pa (10 mTorr). Under the same conditions in an inductively coupled GEC cell, similar values of T_e were measured.³⁸

C. Solving the model

Equations (1), (2), and (4) were solved numerically on a spatial grid of 200 points, covering a distance of 0.5–1.1 mm. Depending on rf bias frequency, we used 2500–10 000 time steps, covering a total time of 1.2–10 rf bias periods, with 1000–4000 time steps per rf bias period. The solution proceeds as follows. At each time step, $W(t)$ is determined by numerically integrating Eq. (4), starting at the surface of the grounded electrode, until the appropriate value is obtained for the voltage drop across the sheath. Once $W(t)$ is known, the electric field is calculated from Eq. (4). Then ion velocities and densities are updated using Eqs. (1) and (2).

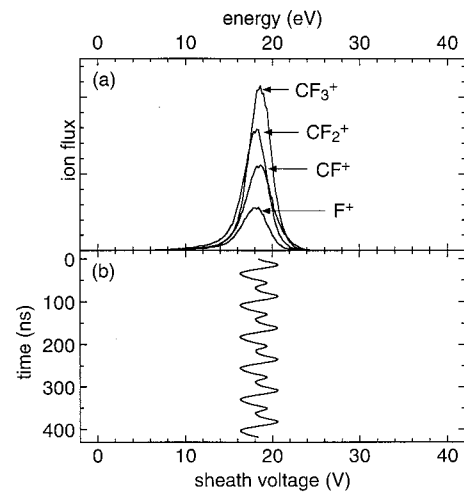


FIG. 3. (a) Measured ion energy distributions and (b) sheath voltage for a 1.33 Pa (10 mTorr) CF_4 discharge at 200 W inductive source power and no rf bias.

Finally, we update the histograms that record the kinetic energy distributions of ions arriving at the grounded surface.

At the first time step, the ion densities and velocities are assumed, quite unrealistically, to be constant in space, but they rapidly converge on a realistic, periodic solution after a number of time steps comparable to the time it takes ions to cross the sheath. Contributions to the ion kinetic energy distributions are only recorded during the final rf cycle of the simulation. They are not recorded during the time that the simulation is converging.

D. Broadening effects

Two effects that cause broadening in measured IEDs are not included in the model, but are accounted for afterward, by operating on the IEDs output by the model. These two effects can be quantified by considering IEDs measured at zero rf bias. As shown in Fig. 3(a), such IEDs have a shape that is nearly Gaussian, with a FWHM of 3.4 eV. Part of this width is contributed by an instrumental broadening of 1 eV inherent in the ion energy analyzer. The remainder is due to the residual capacitive coupling of the inductive plasma source. Even when the electrostatic shield is present, the source still induces a small oscillation in the plasma potential at 13.56 MHz and its harmonics, as shown in Fig. 3(b). Because of this oscillation, ions collected at different times will have slightly different energies, resulting in a broadening of the energy distributions.

We account for the broadening effects as follows. Before the plasma potential wave forms measured by the capacitive probe are input into the model, they are digitally filtered to remove Fourier components at 13.56 MHz and its harmonics, as shown in Fig. 4(b). Then, the IEDs output by the model are convolved with a Gaussian function (with a FWHM of 3.4 eV) which accounts for both broadening effects simultaneously. The effect of the convolution is illustrated in Fig. 4(a). Before the convolution, the IED has very sharp peaks. The apparent intensities of such peaks sometimes depend sensitively on the bin size used in the model

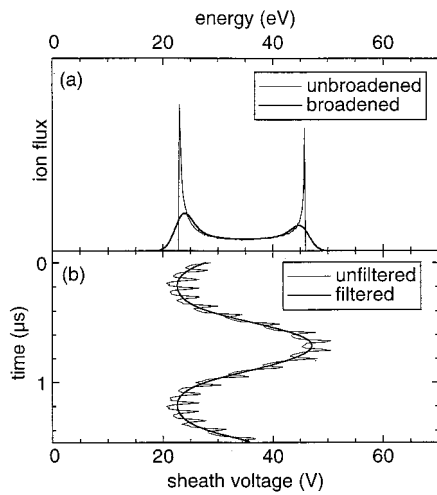


FIG. 4. (a) Model ion energy distribution before (fine line) and after (bold line) convolving the distribution with a Gaussian broadening function. (b) Corresponding sheath voltage wave form as measured (fine line) and after digital filtering (bold line). Results are for CF_3^+ , at 200 W inductive source power, and 1 MHz rf bias.

calculation. The convolution removes any bin size effects and results in IEDs with peaks whose intensity can be more easily compared to measurements.

Alternatively, one could input the unfiltered plasma potential wave forms into the model and do a convolution that only accounts for the instrumental broadening. Such an approach is, however, much less convenient. Unless 13.56 MHz is an exact multiple of the rf bias frequency, the unfiltered wave forms will not have a periodicity equal to one rf bias period. Instead, they will repeat themselves only after a much longer time period lasting many rf cycles. Performing simulations over such a long time period is inefficient and unnecessary.

IV. ION ENERGY DISTRIBUTIONS

Measured ion energy distributions at 200 W inductive source power are compared to model IEDs in Figs. 5–7. Each figure shows results for a different rf bias frequency and several different settings of the rf bias amplitude, as indicated by the values given for V_{pp} , the peak-to-peak voltage across the ground sheath. Each subfigure shows IEDs from four different ionic species: CF_3^+ , CF_2^+ , CF^+ , and F^+ , in order of decreasing intensity. Data within each subfigure are plotted on the same vertical scale, but to make all the IEDs clearly visible it was necessary to vary the vertical scale from one subfigure to another.

A. Low bias frequency

Figure 5 shows results for the lowest rf bias frequency, 100 kHz. Measured IEDs are shown in Figs. 5(a)–5(d); model IEDs are shown in Figs. 5(e)–5(h). All of them show a double-peaked structure, unlike the single peaks observed at zero rf bias [Fig. 3(a)]. As the rf bias amplitude and the peak-to-peak ground sheath voltage increase, the position of the higher energy peak shifts upward in energy, but the lower energy peak hardly shifts at all. The energies of the peaks in

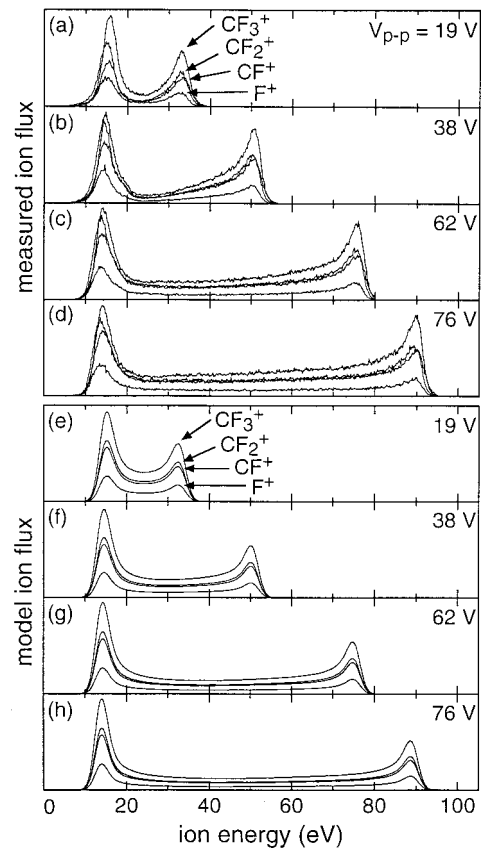


FIG. 5. (a)–(d) Measured and (e)–(h) model ion energy distributions for a bias frequency of 100 kHz and varying bias amplitudes, indicated by values of V_{pp} , the peak-to-peak voltage across the ground sheath. Within each subfigure, distributions for CF_3^+ , CF_2^+ , CF^+ , and F^+ are plotted on a single, arbitrary vertical scale. The distribution with greatest intensity is always CF_3^+ , followed in order by CF_2^+ , CF^+ , and F^+ . The inductive source power is 200 W.

the model IEDs and measured IEDs are in good agreement. For the measurements as well as the model results, the peak energies vary little from one ion to another.

To enable closer comparisons, the energy of the high energy peak, E_{high} , and the energy of the low energy peak, E_{low} , are plotted in Fig. 8(a). Measured values are plotted using symbols; model values are plotted with dotted lines. At 100 kHz, E_{high} and E_{low} do not depend on ion mass, so measured values for different ions fall on top of one another, and model values for different ions fall on the same dotted curve. The model values agree with the measurements.

At 100 kHz, there is a close correlation between the ion energy distributions and the sheath voltage. To see this, the minimum and maximum values of the sheath voltage, V_{min} and V_{max} , have been converted to energies (eV_{min} and eV_{max}) and plotted as solid lines in Fig. 8(a). For both the measurements and the model results, $E_{high} \approx eV_{max}$, and $E_{low} \approx eV_{min}$. This agreement between ion energies and sheath voltages is a well-known property of rf sheaths at low frequencies. If the rf bias frequency is low enough, the rf bias period will be long compared to the time it takes ions to cross the sheath, and ions can be considered to cross the sheath instantaneously. Thus a singly charged ion crossing at time t_0 , when the voltage across the sheath is $V_{gs}(t_0)$, arrives

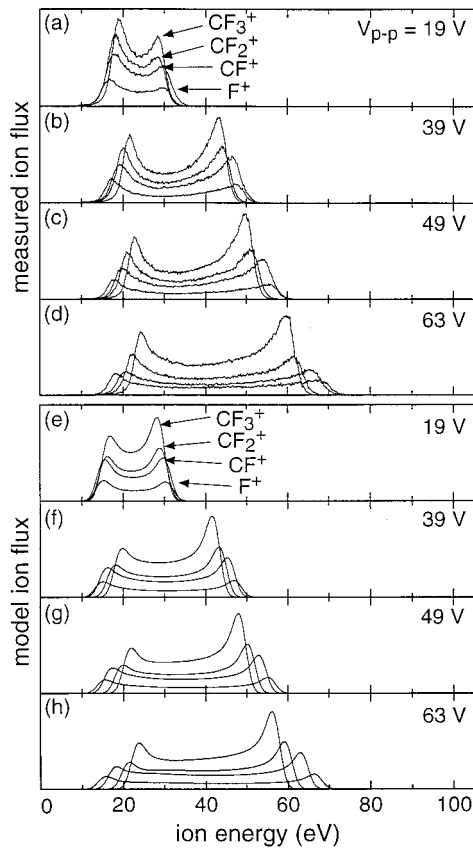


FIG. 6. (a)–(d) Measured and (e)–(h) model ion energy distribution for a bias frequency of 6 MHz and varying bias amplitudes, indicated by values of V_{pp} , the peak-to-peak voltage across the ground sheath. Within each subfigure, distributions for CF_3^+ , CF_2^+ , CF^+ , and F^+ (in order of decreasing intensity) are plotted on a single, arbitrary vertical scale. The inductive source power is 200 W.

at the electrode with an energy of exactly $eV_{gs}(t_0)$. The minimum and maximum ion energies should (in the absence of any broadening effects) exactly equal eV_{min} and eV_{max} . Similarly, the average (mean) ion energy, E_0 , should equal eV_0 , where V_0 is the time-averaged sheath voltage. Plots of E_0 and eV_0 in Fig. 9(a) indeed show that $E_0 \approx eV_0$ for both measured and model values of E_0 .

At low bias frequencies, the shape of the ion energy distributions depends solely on the shape of the sheath voltage wave form. Measured sheath voltage wave forms are quite flat near their minimum or maximum. Therefore ions arriving at the electrode for some time before or after the exact minimum or maximum will have energies close to eV_{min} or eV_{max} . Such ions contribute to the two peaks, one at each end of the distribution. Because the sheath voltage sweeps through intermediate voltages much more rapidly, the intensity of the IED is much lower between the peaks.

In each model IED in Figs. 5(e)–5(h), the amplitude of the lower-energy peak is higher than that of the higher-energy peak. This effect too can be explained by considering the shape of the sheath voltage wave form. Measured sheath voltage wave forms are flatter for a longer time near V_{min} compared to V_{max} .³¹ Therefore more ions arrive at the electrode with energies near eV_{min} than near eV_{max} , resulting in

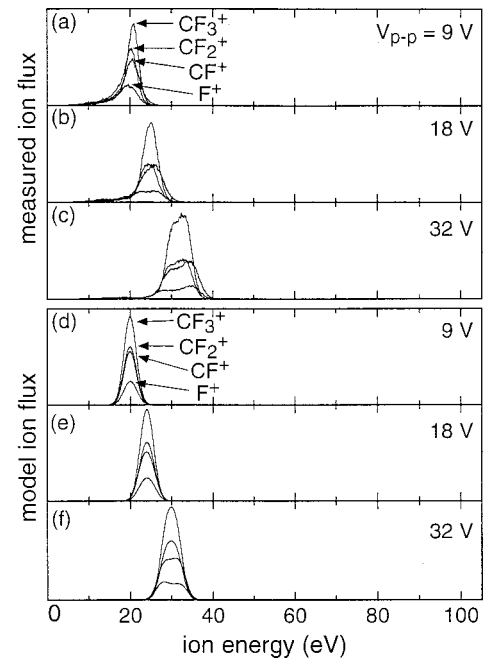


FIG. 7. (a)–(c) Measured and (d)–(f) model ion energy distributions for a bias frequency of 30 MHz and varying bias amplitudes, indicated by values of V_{pp} , the peak-to-peak voltage across the ground sheath. Within each subfigure, distributions for CF_3^+ , CF_2^+ , CF^+ , and F^+ (in order of decreasing intensity) are plotted on a single arbitrary vertical scale. The inductive source power is 200 W.

a more intense lower-energy peak. For the measured IEDs in Figs. 5(a)–5(d), the low energy peaks are more intense than the high energy peaks, but to a lesser degree than that predicted by the model. This disagreement could be caused by the ion energy analyzer discriminating against low energy ions or in favor of high-energy ions. Comparisons indicate that any such discrimination is smaller for the present ion energy analyzer than that used in previous work,¹⁶ but discrimination effects may still be present. Measurements of average ion energies are also affected by discrimination effects, but measured peak energies are rather insensitive.

B. Medium bias frequency

Ion energy distributions obtained at a bias frequency of 6 MHz are shown in Fig. 6. Measured IEDS [Figs. 6(a)–6(d)] and model IEDS [Figs. 6(e)–6(h)] are shown for four different values of V_{pp} , the peak-to-peak sheath voltage. As in Fig. 5, each IED shows a pair of peaks. Unlike Fig. 5, the low-energy peak in Fig. 6 shifts to higher energies for increasing V_{pp} . The shift is greater for heavier ions. The position of the high-energy peak also depends on ion mass, with heavier ions being shifted to lower energies. These shifts are observed in the model results as well as the measurements. For all the ions, and all values of V_{pp} , model predictions for the peak energies agree with measured values.

Figure 8(b) plots 6 MHz results for the positions of the two peaks, E_{high} and E_{low} , and the energies eV_{min} and eV_{max} that correspond to the minimum and maximum sheath voltages. The plots of eV_{min} and eV_{max} are very similar to that seen at 100 kHz, in Fig. 8(a), but the plots of E_{high} and E_{low} are not. Instead of observing $E_{low} \approx eV_{min}$ and E_{high}

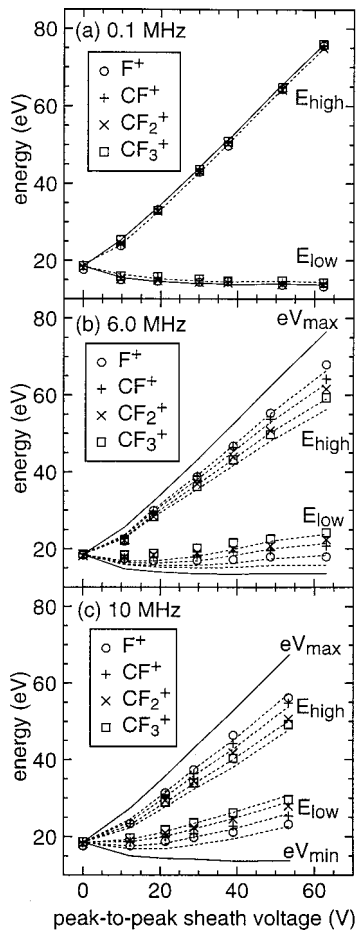


FIG. 8. Measured (symbols) and model (dotted curves) values of E_{high} and E_{low} , the energies of the two peaks in the ion energy distributions, for rf bias at (a) 100 kHz, (b) 6.0 MHz, and (c) 10 MHz. Also plotted (solid curves) are the energies eV_{min} and eV_{max} , where V_{min} and V_{max} are the minimum and maximum values of the sheath voltage. In (a) model values for all four ions are the same, so only one dotted curve is visible.

$\approx eV_{max}$, we instead see that E_{high} is shifted significantly down from eV_{max} and E_{low} is shifted up from eV_{min} . The shifts are greater for heavier ions. When the bias frequency is increased from 6 to 10 MHz, in Fig. 8(c), E_{high} is shifted further down from eV_{max} and E_{low} is shifted further up from eV_{min} . In both Figs. 8(b) and 8(c), model values for E_{high} and E_{low} for different ions, plotted by dotted lines, fall in the same order as the measured values, with lighter ions having higher values of E_{high} and lower values of E_{low} . For all conditions, model values of E_{high} and E_{low} agree with the measurements.

At 6 and 10 MHz, the rf bias period (167 or 100 ns) is comparable to the time that it takes ions to cross the sheath (50–130 ns). Consequently, ions can no longer be considered to cross the sheath instantaneously, absorbing an energy determined by the instantaneous sheath voltage. Instead, they absorb an energy given by an average value of the sheath voltage, averaged over the time during which they are crossing the sheath. This averaging causes an increase in the minimum ion energy and a decrease in the maximum ion energy. These effects are larger for heavier ions because they have

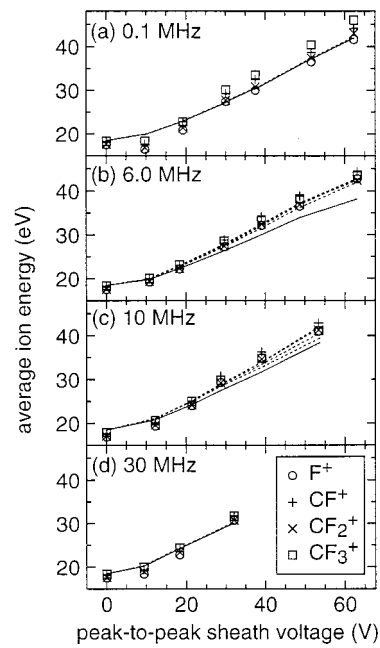


FIG. 9. Measured (symbols) and model (dotted curves) values of E_0 , the average ion energy, for rf bias at (a) 100 kHz, (b) 6.0 MHz, (c) 10 MHz, and (d) 30 MHz. Also plotted (solid curves) is eV_0 , where V_0 is the average value of the sheath voltage. In (a) and (d) model values for all four ions are the same, so only one dotted curve is visible.

longer transit times, and are thus subjected to more averaging.

Comparison of the peak heights in Figs. 5 and 6 shows an increase in the height of the higher energy peak when the rf bias frequency is increased from 100 kHz to 6 MHz. At 100 kHz (Fig. 5) the height of the high energy peak, for measured as well as calculated IEDs, is always less than that of the lower energy peak. In contrast, at 6 MHz (Fig. 6) the height of the high energy peak is often higher than that of the low energy peak, especially for CF_3^+ distributions at high V_{pp} . For lighter ions or lower sheath voltages, the height of the high energy peak is less than that of the low energy peak, but it is nevertheless a greater fraction of the height of the low energy peak than it was at 100 kHz. All IEDs, measured as well as calculated, show this increase in the relative height of the high energy peak.

The changes in peak heights in Figs. 5 and 6 are related to a time-variation in the current and flux of ions during the rf cycle, which occurs whenever the rf bias period becomes comparable to ion transit times.^{1–3} During the portion of the rf cycle when the sheath voltage is increasing, each ion entering the sheath is accelerated slightly faster than the ions that preceded it. Ions “gain on” their predecessors, resulting in a relatively high flux of high energy ions arriving at the electrode near the time that the sheath voltage is maximized. In contrast, when the sheath voltage is decreasing, ions crossing the sheath lag behind their predecessors, resulting in an interval, occurring near the time when the sheath voltage is minimized, during which relatively few ions arrive at the electrode. Consequently there are more higher energy ions to contribute to the higher energy peak and fewer low energy

ions to contribute to the low energy peak than there would be if ions crossed the sheath instantaneously.

The increase in the relative intensity of the high-energy peak is accompanied by an increase in the average ion energy, E_0 . If the flux of each ionic species were constant in time, each would have an average energy equal to eV_0 , where V_0 is the time-averaged sheath voltage. In Figs. 9(b) and 9(c), however, measurements (symbols) and model values (dotted lines) of E_0 are higher than eV_0 (solid line), by as much as 12%–16%.

The increase in average ion energy implies an increase in the power absorbed by ions. The oscillation of ion current, because it is in phase with the sheath voltage,¹ allows ions to absorb more power than they would if their flux were constant in time. Evidence for this increased power absorption has been found in previous studies of high-density argon discharges.^{9,31,39} At frequencies of 10 or 13.56 MHz, measured rf bias powers were as much as 40% higher than the power predicted by models that assume constant ion flux. Energy conservation therefore requires that the average ion energy in such discharges be 40% higher than eV_0 . However, such large increases in power and average ion energy were only observed at high sheath voltages typical of the sheath at the rf biased electrode. At lower voltages, comparable to the ground sheath voltages in Figs. 9(b) and 9(c), the increase in ion power and average ion energy was smaller, 20% or less,³⁹ which is comparable to the increase seen in Figs. 9(b) and 9(c).

One exception to the generally very good agreement between measurements and model results is seen at the lowest sheath voltage, $V_{pp}=19$ V in Fig. 6. In the measured IEDs in Fig. 6(a), the low energy peaks have a larger amplitude than the high energy peaks, but in the CF_3^+ and CF_2^+ model IEDs in Fig. 6(e), the high energy peaks are larger than the low energy peaks. This discrepancy may result from the model's simplified treatment of the electron profile and the presheath boundary in Eqs. (4)–(8), which works better at higher sheath voltages. Further measurements and modeling of IEDs at low sheath voltages could help to resolve this discrepancy and perhaps improve the model. Low sheath voltages are relatively uninteresting from a practical point of view, however, since actual plasma etching processes require higher voltages, ~ 50 V or more, to produce the needed energetic ions.

C. High bias frequency

Ion energy distributions obtained at a bias frequency of 30 MHz are shown in Fig. 7. Measured IEDs [Figs. 7(a)–7(c)] and model IEDs [Figs. 7(d)–7(f)] are shown for three different values of V_{pp} , the peak-to-peak sheath voltage. The narrowing of the IEDs observed when going from 100 kHz to 6 MHz (Figs. 5 and 6) continues further when the frequency is increased to 30 MHz. Indeed, at the lower voltages in Fig. 7, the IEDs have narrowed so much that the two peaks can no longer be distinguished. At the largest voltage, $V_{pp}=32$ V, the two peaks are just beginning to be resolved.

The model IEDs appear slightly less broad than the measured IEDs, but there is nevertheless good agreement in the peak positions.

The results in Fig. 7 indicate that, at 30 MHz, the sheath is entering the high-frequency regime, where the time it takes ions to cross the sheath is much longer than the rf bias period. Therefore the effects of rf electric fields on ion motion are nearly entirely averaged out. Ions can be considered to only follow the dc electric fields. Thus, all ions, regardless of the time that they enter the sheath, absorb an energy equal to eV_0 , where V_0 is the dc voltage across the sheath. Indeed, in all cases in Fig. 7 the centers of the IEDs appear close to eV_0 , which is 20, 24, and 30 V for V_{pp} equal to 9, 18, and 32 V, respectively. Plots of average ion energy in Fig. 9(d) are similarly in good agreement with eV_0 . Strictly speaking, even at 30 MHz the effect of the rf fields is not totally averaged out. The breadth of some of the IEDs, particularly the F^+ IEDs in Figs. 7(c) and 7(f), indicates that the rf bias voltage is still having an effect on the ion energy.

The range of peak-to-peak sheath voltage, V_{pp} , in Fig. 7 is rather limited. We were not able to perform measurements at values of V_{pp} greater than 32 V, because, at 30 MHz (and other high frequencies) nearly all of the rf bias voltage is dropped across the sheath at the biased electrode, and only a small fraction is dropped across the ground sheath. At high frequencies the sheaths have a capacitive impedance that depends very sensitively on electrode area.¹⁶ The reactor has more grounded area than powered area, so the ground sheath impedance is much smaller than the powered sheath impedance. Therefore the ground sheath voltage is only a small fraction of the total rf bias voltage. At lower frequencies, however, the sheaths have a resistive impedance that depends less strongly on electrode area,¹⁶ and a larger fraction of the voltage is dropped across the ground sheath. Thus, at 6 MHz, peak-to-peak ground sheath voltages up to 63 V could be obtained, and at 100 kHz, V_{pp} higher than 100 V could be obtained.

The inability to obtain high ground sheath voltages at 30 MHz is not a very serious limitation of our model validation, because at 30 MHz the sheath model predicts relatively simple and uninteresting IEDs. More serious is the inability to obtain voltages $V_{pp}>63$ V at 6 MHz. At 6 MHz, the model predicts complicated, time-dependent ion dynamics effects at high voltages, e.g., large increases in E_0 over eV_0 , that we would like to validate. To perform such validations would require ion energy measurements at the rf biased electrode, or a different plasma reactor with a more symmetrical ratio of biased area to grounded area.

V. WIDTH OF ENERGY DISTRIBUTIONS

The energy spread or width of an ion energy distribution is a particularly important parameter that has been studied extensively in previous experimental^{4,14,16–19,21–23} and modeling^{4,6,9,13–15} work. Several different definitions for the width have been used. Here, we define the width to be the separation between the two peaks,

$$\Delta E = E_{\text{high}} - E_{\text{low}}. \quad (9)$$

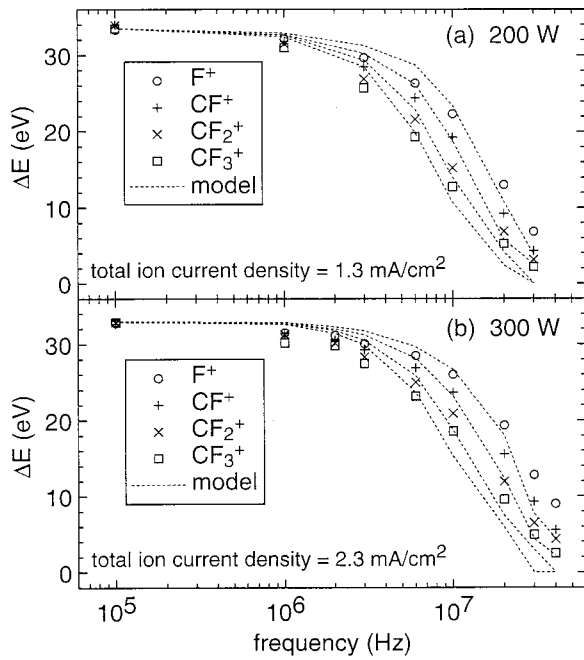


FIG. 10. Measured (symbols) and model (dotted curves) values of ΔE , the separation between the two peaks in the ion energy distributions, as a function of rf bias frequency at an inductive source power of (a) 200 W and (b) 300 W, for a constant peak-to-peak sheath voltage, $V_{pp} = 35$ V.

For conditions where only a single peak is observed, ΔE is defined to be zero.

A. Results

The qualitative behavior of ΔE can be determined from the behavior of E_{high} and E_{low} in Fig. 8. Examination of the data shows that ΔE varies roughly linearly with V_{pp} , the peak-to-peak amplitude of the sheath voltage. At constant V_{pp} , ΔE declines as the rf bias frequency is increased.

The frequency dependence of ΔE is shown in detail in Fig. 10(a). All the values of ΔE shown there are at a constant peak-to-peak sheath voltage, $V_{pp} = 35$ V, obtained by interpolating or extrapolating ΔE values from nearby voltages. For each of the four ionic species, measured values of ΔE , plotted as symbols, show a similar decline in ΔE with frequency. Model values of ΔE for the same four ions are plotted as dotted curves, which fall in the same order as the measured points and track them rather closely. Nevertheless, some consistent deviations from the measurements are seen. The model tends to overestimate ΔE at 1–3 MHz and underestimate it at 20–30 MHz.

We also studied the dependence of ΔE on inductive source power. In general, changes in inductive source power have two effects on ion energy distributions. First, as in previous studies of argon discharges,^{16,25,40} increasing the inductive source power increases the plasma potential measured at zero rf bias by about 1 V.²⁵ Ion energies measured at zero rf bias are therefore shifted up by about 1 eV.⁴⁰ IEDs measured with rf bias applied are also shifted up by the same amount.¹⁶ This effect tends to shift the positions of both peaks, E_{high} and E_{low} , by the same amount, so there is little or no effect on ΔE . Second, for higher inductive source powers, the narrowing of ΔE occurs at higher frequencies. This effect is

visible in Fig. 10(b), which shows a plot similar to Fig. 10(a), but at an inductive source power of 300 W, instead of 200 W. The shape of the ΔE vs frequency plots in Figs. 10(a) and 10(b) are nearly identical. The only difference between them is that the latter are shifted horizontally to higher frequencies. To obtain the same value of ΔE , a higher frequency is required at 300 W than at 200 W. At higher inductive power, the plasma density and total ion current density are higher, and, for a constant sheath voltage, the sheath is thinner, and ion transit times are shorter. Thus the narrowing of ΔE , which depends on the rf bias period becoming comparable to the ion transit time, is shifted to shorter rf periods, i.e., higher rf frequencies, when the inductive power is increased. This effect, noted in previous modeling studies,^{11,13} is analyzed quantitatively in the next section.

B. Analysis

Here, we calculate ion transit times using a simple, dc, Child–Langmuir sheath model, as in previous work.^{6,16} In such models, the density of any ionic species is given by

$$n_i = (J_i/e)[m_i/(2eV)]^{1/2}, \quad (10)$$

where m_i and J_i are its mass and its time-averaged current density, and V is the electrostatic potential, here measured with respect to the plasma. The total ion density, n_+ , is obtained by summing over all ionic species

$$n_+ = \sum_{i=1}^N \frac{J_i}{e} \left(\frac{m_i}{2eV} \right)^{1/2} = \frac{J_+}{e} \left(\frac{m^*}{2eV} \right)^{1/2}, \quad (11)$$

where J_+ is the total time-averaged ion current density and m^* is an average ion mass defined by

$$(m^*)^{1/2} J_+ = \sum_{i=1}^N m_i^{1/2} J_i. \quad (12)$$

Solving Eq. (11) and Poisson’s equation simultaneously, we obtain the relation between potential V and position x :

$$x = 2/3(2e/m^*)^{1/4}(\epsilon_0/J_+)^{1/2}V^{3/4}. \quad (13)$$

This result is the same as the Child–Langmuir law for a single ionic species except that the single ion mass is replaced by m^* . Following previous derivations,^{6,16} ion transit times are then derived from Eq. (13). We obtain the transit time of the i th ion, τ_i , as

$$\tau_i = 2[V/(2em^*)]^{1/4}(m_i\epsilon_0/J_+)^{1/2}. \quad (14)$$

For the voltage V we insert the peak-to-peak sheath voltage, V_{pp} , and then take the ratio of τ_i to the rf bias period, $T = 1/f$, where f is the rf bias frequency, to obtain

$$\tau_i/T = 2[V_{pp}/(2em^*)]^{1/4}(m_i\epsilon_0/J_+)^{1/2}f. \quad (15)$$

The parameter τ_i/T is proportional to f , but is dimensionless. It defines a normalized, dimensionless frequency scale.

In Fig. 11(a), the ΔE data from Fig. 10 are plotted against τ_i/T . Plotted in the figure are all the values at 200 W from Fig. 10(a) and all the values at 300 W from Fig. 10(b). Also plotted is a fifth ion of mass 28 amu which was measured at 300 W and was included in the 300 W simulation but was not shown in Fig. 10(b) for the sake of clarity. When

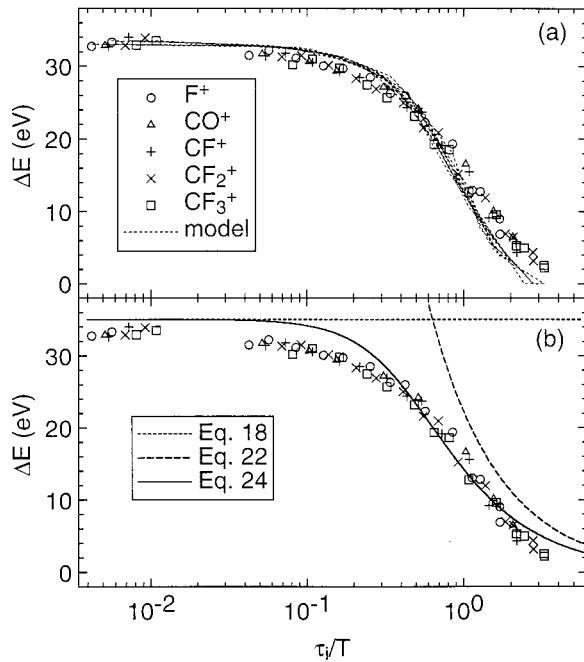


FIG. 11. (a) Measured (symbols) and model (dotted curves) values of the peak separation, ΔE , from Fig. 9 plotted as a function of τ_i/T , the ratio of the ion transit time to the rf bias period. (b) The same measurements in (a) compared to three analytic models.

plotted versus τ_i/T , the measured values of ΔE fall onto a single curve. The model values of ΔE also fall onto a single curve, which is slightly different from the measured curve. Each curve has a vertical width comparable to the ± 1 eV uncertainties of the measured and model values. Both curves are smooth. The gaps between data seen in Fig. 10 are nearly all filled in, except for one gap in an uninteresting region near $\tau_i/T=0.02$. With the gaps filled, one can see more clearly how the model tends to overestimate ΔE in the middle of the plot, at $\tau_i/T \approx 0.2$, and underestimate ΔE at higher values, near $\tau_i/T \approx 2$.

The collapse of ΔE onto a single curve indicates that ΔE depends only on the ratio τ_i/T , not on the individual variables like m_i and J_+ that make up τ_i/T . Furthermore, according to Eq. (15), changes in m_i and J_+ only affect τ_i/T by causing a multiplicative shift in the frequency scale. Thus plots of ΔE vs log frequency for different ion masses should all have the same shape and be shifted horizontally by an amount that varies according to $m_i^{-1/2}$, as can be verified by examining the original data in Fig. 10. Similarly, if the only effect of changing the source power is a change in J_+ , then values for ΔE at different powers should have the same shape but be displaced horizontally by an amount that varies as $J_+^{1/2}$. This too can be verified by comparing the original data in Fig. 10(a), where $J_+=1.3$ mA/cm², to Fig. 10(b), where $J_+=2.3$ mA/cm².

In a previous experiment,¹² ΔE versus frequency curves of different ions were shifted by an amount proportional to the inverse *fourth* root of ion mass. There is no contradiction, however, since that study did not compare different ions in the same discharge, but instead compared ions in different gases (at constant J_+). The rare gases used in that study each

have a single dominant ion whose mass can also be considered the average ion mass, m^* . Thus the $(1/m^*)^{1/4}$ and $m_i^{1/2}$ dependences in Eq. (15) combine to give a fourth root dependence on mass, and the ΔE curves are shifted by the inverse fourth root of mass.

The shifts seen in Fig. 10 can also be explained by considering ion plasma frequencies, instead of ion transit times. Using Eq. (11), the plasma frequency of the i th ion is

$$\omega_i = (n_+ e^2 / m_i \epsilon_0)^{1/2} = (J_+ / m_i \epsilon_0)^{1/2} (em^* / 2V)^{1/4}. \quad (16)$$

We evaluate ω_i at the Bohm point, x_B , where $V(x_B) = 0.5kT_e/e \equiv V_B$, k is Boltzmann's constant and T_e is the electron temperature. Then we use $\omega_i(x_B)$ to define another normalized, dimensionless frequency scale,

$$\omega / \omega_i(x_B) = 2\pi(2V_B / em^*)^{1/4} (m_i \epsilon_0 / J_+)^{1/2} f, \quad (17)$$

where $\omega = 2\pi f$ is the angular frequency. Comparing Eqs. (15) and (17), we see that $\omega / \omega_i(x_B)$ has the same dependence on m^* , m_i , and J_+ as τ_i/T . Indeed, for constant voltage, $\omega / \omega_i(x_B)$ and τ_i/T are the same except for a constant multiplicative factor. Here, $\omega / \omega_i(x_B) = 2.25\tau_i/T$. Thus all the arguments based on τ_i/T also follow from analysis of $\omega / \omega_i(x_B)$.

C. Discussion

Several previous studies^{4,13,16,21} present plots similar to Fig. 11(a). In one,¹³ the widths of calculated IEDs are plotted versus τ_i/T . The resulting curve is very similar in shape to that in Fig. 11(a). The position of the curves also agree: in Ref. 13, as in Fig. 11(a), the point of steepest slope occurs at $\tau_i/T \approx 1$. In Ref. 4, the peak separation ΔE was plotted versus $\omega\tau_i$, again yielding a curve with a shape similar to Fig. 11(a). The point of steepest slope, observed at $\omega\tau_i \approx 2\pi$, also agrees. In one experimental study,¹⁶ a plot of measured values of ΔE versus τ_i/T has a similar slope to that of Fig. 11(a), but its position is shifted horizontally. Presumably, those data are shifted because the ion current density, J_+ , was not measured in that study. Instead, only a rough estimate for J_+ , based on measurements made in another plasma reactor, was used. In another experiment,²¹ Langmuir probe measurements of electron density were used to define ion transit times to generate a plot of measured IED width versus $(T/\tau_i)^2$. That plot appears to disagree with Fig. 11(a), but it is hard to say for sure, since the equations that define τ_i in that study were not completely specified. A subsequent analysis¹³ of those data shows them to be in agreement.

Several models are simple enough to predict an analytic relation between ΔE and τ_i/T . In Fig. 11(b), we compare these analytic relations to the data from Fig. 11(a). Simplest of all are low frequency models, which predict a constant ΔE ,

$$\Delta E = eV_{pp}, \quad (18)$$

which is plotted as the horizontal dotted line in Fig. 11(b). This equation is fairly accurate for τ_i/T below about 0.1. There, measured values of ΔE are seen to be rather independent of τ_i/T . At $\tau_i/T > 0.1$, however, measured ΔE values rapidly fall away from Eq. (18). The range $\tau_i/T < 0.1$ where Eq. (18) is valid roughly corresponds to frequencies $f < 1$

MHz. This range is comparable to the ranges where low-frequency behavior was observed in previous experiments in low-density²² and high-density¹⁶ argon discharges.

Even at the lowest values of τ_i/T in Fig. 11(b), the measurements fall about 2 eV below Eq. (18), because Eq. (18) does not account for broadening effects. IEDs predicted by models usually fall vertically to zero at their minimum and maximum energies, as shown in Fig. 4(a), producing peaks with a very asymmetric, triangular shape. When these asymmetric peaks are broadened, the maxima are shifted inward [again, see Fig. 4(a)] resulting in a decrease in ΔE .

A second analytic equation for ΔE , derived for high rf bias frequencies, has been reported in several papers.^{6,14,15} Assuming a sinusoidal sheath voltage,

$$V = V_0 + V_1 \sin \omega t, \tag{19}$$

they obtain

$$\Delta E = (8eV_1/3\omega d)(2eV_0/m_i)^{1/2}, \tag{20}$$

where d is the sheath width. Kawamura *et al.*⁶ further simplify this equation to obtain

$$\Delta E = (4eV_1/\pi)(\tau_i/T)^{-1} = (2eV_{pp}/\pi)(\tau_i/T)^{-1}. \tag{21}$$

Substituting the peak-to-peak sheath voltage, $V_{pp} = 2V_1$, and τ_i from Eq. (14),

$$\begin{aligned} \Delta E &= (2eV_{pp}/\pi)(\tau_i/T)^{-1} \\ &= (e/\pi)(2em^*)^{1/4}(J_+/m_i\epsilon_0)^{1/2}V_{pp}^{3/4}f^{-1}. \end{aligned} \tag{22}$$

This equation is plotted as a dashed curve in Fig. 11(b). Agreement with measurements is fairly good for $\tau_i/T > 1$. There, measured values of ΔE do vary roughly as $(\tau_i/T)^{-1}$, as Eq. (22) predicts. At $\tau_i/T < 1$, however, Eq. (22) rapidly diverges from the measurements. The range $\tau_i/T > 1$ where Eq. (22) is valid roughly corresponds to frequencies greater than 10–20 MHz. Experiments in capacitively coupled discharges have also confirmed the inverse dependence of ΔE on frequency in Eqs. (20)–(22) over a comparable frequency range, $f \geq 20$ MHz.¹⁴

Equation (22) predicts that ΔE is proportional to the inverse square root of the ion mass. This $m_i^{-1/2}$ dependence has been observed experimentally in low density discharges at frequencies of 13.56 MHz^{17,23} and 65 MHz.¹⁴ Close examination of the ΔE measurements in Fig. 10 shows that they also roughly follow this $\Delta E \propto m_i^{-1/2}$ dependence, but only at frequencies greater than 10–20 MHz, i.e., at $\tau_i/T > 1$. Below 10–20 MHz, the dependence of ΔE on m_i becomes weaker until, at 1 MHz and below, ΔE becomes essentially independent of ion mass. At some intermediate frequencies between 1 and 10 MHz, ΔE for the heavier ions still roughly obey Eq. (22), but the lighter ions do not. Similar results were observed in an Ar/C₄F₈/O₂ discharge with rf bias at 2 MHz, where the $m_i^{-1/2}$ dependence was observed for heavier ions, but a weaker dependence was seen for lighter ions.¹⁸ Sometimes, if a mass spectrometer is not available, an assumed $\Delta E \propto m_i^{-1/2}$ dependence is used to identify the ionic species that contribute to each peak in mass-integrated IEDs.^{19,41} But this practice is only recommended at $f > 10$ MHz or $\tau_i/T > 1$, where the $\Delta E \propto m_i^{-1/2}$ relation is valid.

A final analytic equation for ΔE can be obtained using the “effective potential” method of Ref. 9. For each ionic species, an effective potential, V_i , can be defined by the equation

$$\partial V_i / \partial t = -\omega_i(x_B)(V_i - V). \tag{23}$$

This equation states that V_i is a damped version of the true potential, V , and the characteristic frequency of the damping is just the ion plasma frequency, ω_i , which we have chosen to evaluate at the Bohm point, x_B , as in Eq. (17). Each ion is assumed to be in equilibrium with V_i , and thus ΔE is equal to the peak-to-peak amplitude of V_i . For sinusoidal $V(t)$, we solve Eq. (23) for $V_i(t)$ and use Eqs. (15) and (17) to obtain

$$\begin{aligned} \Delta E &= eV_{pp}\{1 + [\omega/\omega_i(x_B)]^2\}^{-1/2} \\ &= eV_{pp}[1 + (2.25\tau_i/T)^2]^{-1/2}. \end{aligned} \tag{24}$$

A result nearly identical to this equation has been obtained by Charles *et al.* (Eq. 18 of Ref. 4) from an analytical fit of numerical model results.

In Fig. 11, Eq. (24) is plotted as a solid curve. The curve agrees rather well with ΔE measurements over the entire range of ω/ω_i . In the low frequency limit, $\omega/\omega_i \ll 1$, Eq. (24) approaches Eq. (18). Like Eq. (18), Eq. (24) slightly overestimates ΔE for the lowest frequencies because of broadening effects discussed above. In the high-frequency limit, $\omega/\omega_i \gg 1$, Eq. (24) becomes $\Delta E = eV_{pp}\omega_i/\omega$, which is identical to Eq. (22), except for a constant multiplicative factor. Comparison of Figs. 11(a) and 11(b) shows that Eq. (24) provides predictions for ΔE over the entire frequency range, from $\omega/\omega_i \ll 1$ to $\omega/\omega_i \gg 1$, that are nearly as accurate as the numerical sheath model. The effective potential model does not, however, account for the time-variation in ion current and its effect on peak intensities and average ion energies. For those parameters, the numerical sheath model yields more accurate predictions.

VI. CONCLUSIONS

By combining ion energy measurements with capacitive probe measurements of sheath voltage and Faraday cup measurements of total ion current density, rigorous tests of model predictions for ion energy distributions have been performed. The numerical sheath model tested here was found to give accurate predictions for ion energy distributions and their dependence on rf bias frequency, sheath voltage, ion current density, and ion mass. Only a few rather unimportant differences between model and measured IEDs were seen.

Measured IEDs as well as model IEDs show three different types of behavior over different ranges of frequency or of τ_i/T , the ratio of ion transit time to rf bias period. At frequencies below about 1 MHz, where $\tau_i/T < 0.1$, the ions can be considered to cross the sheath instantaneously. Within this low-frequency range, the ion energy distributions do not depend on total ion current density or ion mass; they depend only on the sheath voltage wave form. Two peaks are observed in the distributions. Except for small shifts due to broadening effects, the peak energies are equal to eV_{\min} and eV_{\max} , and the width of the IED is equal to eV_{pp} , where V_{\min} , V_{\max} , and V_{pp} are the minimum, maximum, and peak-

to-peak sheath voltage. The average ion energy is given by eV_0 , where V_0 is the average sheath voltage.

In an intermediate range of frequencies, at 1 MHz $< f < 10$ MHz, or $0.1 < \tau_i/T < 1$, there are still two peaks in the IEDs. However, the lower-energy peak is shifted up from eV_{\min} , the higher-energy peak is shifted down from eV_{\max} , and the width of the distribution is less than eV_{pp} . In this frequency range, the current and flux of ions arriving at the electrode surface varies with time during the rf cycle. This oscillation in ion flux causes an increase in the intensity of the higher-energy peak relative to the lower-energy peak. The average ion energy and the total power absorbed by ions are larger than the values (eV_0 and J_+V_0) that would be predicted if the ion flux were constant in time.

At frequencies above about 10 MHz, where $\tau_i/T > 1$, the IEDs become even narrower. For constant sheath voltage, the IED width is proportional to the reciprocal of the frequency, the square root of the total, time-averaged ion current density, and the inverse square root of the ion mass. As the frequency is increased, the IED eventually narrows so much that it is difficult to resolve the high-energy and low-energy peaks; only a single peak is observed. The oscillation in ion flux reaches a maximum at intermediate frequencies, i.e., at $\tau_i/T \approx 1$, and then it rapidly becomes insignificant at $\tau_i/T > 1$. Thus at high frequencies the average ion energy is again simply equal to eV_0 .

Some simple analytic models give rather accurate predictions for IED width across the entire frequency range. They do not, however, predict the changes in peak intensities and average ion energy seen at intermediate frequencies. To predict such effects requires a model that allows the ion flux to vary with time, like the numerical model tested here. Further study of the intermediate frequency range would be worthwhile, either at high sheath voltages, which we were not able to obtain in this study, or at low sheath voltages, where the model's treatment of the plasma/sheath boundary may need improvement. Further studies performed at higher pressures, where ion collisions in the sheath become important, would also be worthwhile, and would allow testing of collisional models.

¹M. A. Sobolewski, Phys. Rev. E **62**, 8540 (2000).

²D. Bose, T. R. Govindan, and M. Meyyappan, J. Appl. Phys. **87**, 7176 (2000).

- ³Y. D. Lee, S. S. Kim, S. H. Ku, and C. S. Chang, Phys. Plasmas **7**, 766 (2000).
- ⁴C. Charles, A. W. Degeling, T. E. Sheridan, J. H. Harris, M. A. Lieberman, and R. W. Boswell, Phys. Plasmas **7**, 5232 (2000).
- ⁵S. Rauf, J. Appl. Phys. **87**, 7647 (2000).
- ⁶E. Kawamura, V. Vahedi, M. A. Lieberman, and C. K. Birdsall, Plasma Sources Sci. Technol. **8**, R45 (1999).
- ⁷E. A. Edelberg and E. S. Aydil, J. Appl. Phys. **86**, 4799 (1999).
- ⁸T. Panagopoulos and D. J. Economou, J. Appl. Phys. **85**, 3435 (1999).
- ⁹P. A. Miller and M. E. Riley, J. Appl. Phys. **82**, 3689 (1997).
- ¹⁰N. Mizutani and T. Hayashi, Jpn. J. Appl. Phys., Part 2 **36**, L1470 (1997).
- ¹¹R. J. Hoekstra and M. J. Kushner, J. Appl. Phys. **79**, 2275 (1996).
- ¹²D. Martin and H. Oechsner, Vacuum **47**, 1017 (1996).
- ¹³M. S. Barnes, J. C. Forster, and J. H. Keller, IEEE Trans. Plasma Sci. **19**, 240 (1991).
- ¹⁴Y. Okamoto and H. Tamagawa, J. Phys. Soc. Jpn. **29**, 187 (1970).
- ¹⁵P. Benoit-Cattin and L. C. Bernard, J. Appl. Phys. **39**, 5723 (1968).
- ¹⁶M. A. Sobolewski, J. K. Olthoff, and Y. Wang, J. Appl. Phys. **85**, 3966 (1999).
- ¹⁷O. Tsuda, Y. Tatebayashi, Y. Y. Takamura, and T. Yoshida, Plasma Sources Sci. Technol. **8**, 392 (1999).
- ¹⁸Y. Hikosaka, H. Hayashi, M. Sekine, H. Tsuboi, M. Endo, and N. Mizutani, Jpn. J. Appl. Phys., Part 1 **38**, 4465 (1999).
- ¹⁹E. A. Edelberg, A. Perry, N. Benjamin, and E. S. Aydil, J. Vac. Sci. Technol. A **17**, 506 (1999).
- ²⁰N. Mizutani, Y. Nagata, A. Kubo, and T. Hayashi, Rev. Sci. Instrum. **69**, 1918 (1998).
- ²¹W. M. Holber and J. Forster, J. Vac. Sci. Technol. A **8**, 3720 (1990).
- ²²R. H. Bruce, J. Appl. Phys. **52**, 7064 (1981).
- ²³J. W. Coburn and E. Kay, J. Appl. Phys. **43**, 4965 (1972).
- ²⁴P. J. Hargis, Jr. et al., Rev. Sci. Instrum. **65**, 140 (1994).
- ²⁵P. A. Miller, G. A. Hebner, K. E. Greenberg, P. D. Pochan, and B. P. Aragon, J. Res. Natl. Inst. Stand. Technol. **100**, 427 (1995).
- ²⁶A. Schwabedissen, E. C. Benck, and J. R. Roberts, Phys. Rev. E **55**, 3450 (1997).
- ²⁷R. Jayaraman, R. T. McGrath, and G. A. Hebner, J. Vac. Sci. Technol. A **17**, 1545 (1999).
- ²⁸Y. Wang and J. K. Olthoff, J. Appl. Phys. **85**, 6358 (1999).
- ²⁹M. A. Sobolewski, IEEE Trans. Plasma Sci. **23**, 1006 (1995).
- ³⁰V. A. Godyak and R. B. Piejak, J. Appl. Phys. **68**, 3157 (1990).
- ³¹M. A. Sobolewski, Phys. Rev. E **59**, 1059 (1999).
- ³²M. A. Lieberman, IEEE Trans. Plasma Sci. **16**, 638 (1988).
- ³³V. A. Godyak and N. Sternberg, Phys. Rev. A **42**, 2299 (1990).
- ³⁴D. Bohm, in *The Characteristics of Electrical Discharges in Magnetic Fields*, edited by A. Guthrie and R. K. Wakerling (McGraw-Hill, New York, 1949), p. 77.
- ³⁵R. N. Franklin, J. Phys. D **33**, 3186 (2000).
- ³⁶M. S. Benilov, IEEE Trans. Plasma Sci. **28**, 2207 (2000).
- ³⁷H. Singh and D. B. Graves, J. Appl. Phys. **88**, 3889 (2000).
- ³⁸M. Edamura and E. C. Benck (private communication).
- ³⁹M. A. Sobolewski, J. Appl. Phys. **90**, 2660 (2001).
- ⁴⁰J. R. Woodworth, M. E. Riley, D. C. Meister, B. P. Aragon, M. S. Le, and H. H. Sawin, J. Appl. Phys. **80**, 1304 (1996).
- ⁴¹A. D. Kuypers and H. J. Hopman, J. Appl. Phys. **67**, 1229 (1990).